

# A Vibration Absorber Based on Two-dimensional Acoustic Black Holes

Hongli Ji<sup>1</sup>, Ning Wang<sup>1</sup>, Chao Zhang<sup>1</sup>, Xiaodong Wang<sup>1</sup>, Li Cheng<sup>2</sup>, Jinhao Qiu<sup>1\*</sup>

<sup>1</sup>College of Aerospace Engineering, Nanjing University of Aeronautics and Astronautics, Nanjing 210016, China

<sup>2</sup>Department of mechanical Engineering, Hong Kong Polytechnic University, Hung Hom, Kowloon, Hong Kong

**Abstract:** As a passive damping technique for vibration and noise mitigation, acoustic black hole (ABH) structures have been drawing an increasing attention because of their easy-to-realize and broadband wave focusing and energy dissipation characteristics. Structures with embedded ABHs, however, inevitably compromise the overall structural stiffness and strength, which hampers their use as critical structural components. As an alternative, this paper proposes a new type of device, *i.e.* a two-dimensional circular ABH-based dynamic vibration absorber (2D ABH-DVA), as an auxiliary component to be added to an existing structure for vibration suppressions. Using a plate as benchmark structure, finite element (FE) simulation results show a systematic reduction of its resonant peaks over a broad frequency range upon the deployment of the ABH-DVA. Analyses uncover two underlying mechanisms which dominate the physical process: dynamic interaction with the host structure and damping enhancement as a result of ABH-specific energy trapping. This is warranted by an effective dynamic coupling between the primary structure and the add-on ABH-DVA, which can be quantified by a mode-specific and location-dependent coupling coefficient defined in the paper. It is further demonstrated that, despite the rich modal contents of the ABH-DVA, strong coupling with the primary structure only takes place through a few DVA modes. Analyses also lead to a simple linear relationship relating the overall system damping with the properties of the damping material over the ABH-DVA. Finally, the broadband vibration suppression ability of the proposed 2D ABH-DVA is verified through experiments. The study demonstrates

---

\*Corresponding author.

E-mail addresses: jihongli@nuaa.edu.cn (Hongli Ji), wangning96@nuaa.edu.cn (Ning Wang), li.cheng@polyu.edu.hk (Li Cheng), qiu@nuaa.edu.cn (Jinhao Qiu)

the unique coupling features between the DVA and the host structure, which provides design guidelines for unsymmetrical 2D or other ABH-DVA designs in the future.

**Key words:** Acoustic black hole; vibration control; dynamic vibration absorber; coupling analysis

## 1. Introduction

Structural vibration is a vital problem in transportation vehicles such as aircraft, high-speed trains and cars, etc. due to the use of light-weight materials and structures. As one of the passive damping techniques, acoustic black hole (ABH) structures have been drawing an increasing attention for applications such as vibration and noise control owing to their easy-to-realize and broadband characteristics. In one-dimensional cases, the thickness of an ABH wedge is tailored according to a power-law variation  $h(x) = \varepsilon x^m$ , ( $m \geq 2$ ). As a result, the phase velocity of the flexural waves gradually reduces to zero when approaching the taper edge, thus resulting in zero wave reflection theoretically. In the two-dimensional case, the structure thickness can also be tailored along the radial direction to produce similar phenomena, forming a type of lens which focuses the structure-borne flexural wave energy to a specific location. Through such tailoring and employing a small amount of damping materials within the thinnest part of the ABH region, flexural waves can be efficiently focalized and dissipated, conducive to effective vibration suppressions of the structure.

Existing researches on ABH target several important aspects, ranging from theoretical [1-3] and experimental investigations [4, 5], design improvement [6-7] and optimization [8-10] and engineering applications [11-16]. For the latter, ABHs have been typically explored for vibration suppressions [8-12], noise control [13, 14] and energy harvesting [15, 16]. From the design perspective, ABH indentations are usually embedded into a structure in most applications. Efforts have also been made to conceive various forms of ABH structures which potentially can provide better mechanical properties, which allow for more diversified engineering applications. For example, a new type of beam structure embedded with a double-bladed ABH indentation was investigated from both static and dynamic perspectives [17, 18].

One-dimensional ABH feature was also proposed to be embedded into a turbine blade to achieve vibration control [11]. As to 2D structures, Georgiev *et al.* incorporated a two-dimensional ABH near the focus of an elliptic plate and investigated its vibration characteristics [19]. An experimental investigation was carried by Bowyer *et al.* on the damping characteristics of flexural vibrations in plates containing multiple 2D ABHs [20, 21]. As a typical application, an ABH plate was used as an engine cover for vehicle vibration and noise reduction and a significant noise level reduction was achieved [14]. Meanwhile, Zhao *et al.* designed a piezoelectric energy harvester based on the acoustic black hole principle [15]. Capitalizing on the ABH-specific energy trapping feature, a PZT array covering five ABH cells along a beam was proposed to increase the energy recovery efficiency.

Although promising benefits can be achieved in structures with embedded ABHs, the ABH indentations inevitably reduce the overall stiffness and strength of the structures. When used as critical structural components, this kind of design and structural modification may not be allowed. Recently the idea of add-on ABH-based dynamic dampers, called ABH-featured Resonant Beam Damper (ABH-RBD), was proposed by Zhou and Cheng for the vibration suppression of a beam structure [22]. The proposed ABH-RBD is a short beam with an ABH portion at its end. Attached to the primary beam, the overall stiffness and strength of the host structure retain intact. Through embracing the principles of both dynamic vibration absorbers and waveguide absorbers, the ABH-RBD has been shown to exhibit broadband vibration suppression capability, in contrast to the single-frequency feature of a traditional dynamic absorber which usually requires meticulous tuning to target particular frequencies.

The above study, however, was limited to 1D cases, in which both the primary structure and the add-on ABH-RBD device feature relatively simple modal behavior along the beam direction. Although one can surmise to achieve multi-directional vibration control in a two-dimensional structure like a plate using multiple devices, the increase in number of the device would make the implementation cumbersome and impractical. Therefore, it is practically relevant to investigate the possibility of using a single DVA device to control multi-directional modes of a host plate. It is obvious that a two-dimensional structure like a plate has richer modal frequencies

with multi-directional features. To tackle the problem, this paper reports a new type of ABH-based circular dynamic vibration absorber (2D ABH-DVA). As will be demonstrated later, its design, dynamics and performance differ from the existing ones reported in the literature. The paper targets a twofold objective, thus showing its novelty: to demonstrate the feasibility of using one add-on absorber for the vibration reduction of a 2D structure exemplified by a plate; and to uncover the underlying physical mechanisms behind the vibration suppression phenomena.

The paper contains the following inter-related parts. The proposed 2D ABH-DVA is first described and the vibration suppression ability is demonstrated through the finite element model using Abaqus. For further analyses, a simplified substructuring model is proposed to understand the observed phenomena and the dynamic interaction between the two structural components within specific frequency ranges. Analyses lead to a mode-specific and location-dependent coupling coefficient which allows the quantification of the coupling strength. Vibration control mechanism and the influence of the installation position, characteristic frequency, vibration mode shape of the ABH-DVA and material loss factor of damping layers are discussed based on the proposed simplified coupling model and finite element simulations. Experiments are then conducted. Both Finite Element (FE) simulation and experimental results show that the resonant peaks of the primary system can be effectively suppressed over a broad frequency range. Analyses confirm two vibration suppression mechanisms: dynamic interaction and damping enhancement, imposed on different resonance modes of the primary structure. It is also found that, although the 2D ABH-DVA has very dense and abundant natural modes, only a few of them can be strongly coupled with those of the primary structure because of the selective coupling pattern.

## 2. 2D circular ABH-DVA and simulation model

The proposed 2D circular ABH-DVA is shown in Fig. 1. It is an ABH-featured disk, to which an annular damping layer of a constant thickness  $h_d$  is bonded along its edge. The ABH disk can be divided into three parts: a central uniform circular platform with a constant thickness  $h_0$  (from 0 to  $r_1$ ), a region with a varying thickness (from  $r_1$  to  $r_2$ ) and another platform of constant thickness  $h_1$  (from  $r_2$  to  $r_3$ ). The

thickness profile of the disk along the radial direction can be mathematically defined by

$$h(r) = \begin{cases} h_0, & (0 \leq r \leq r_1) \\ \varepsilon(r - r_2)^m + h_1, & (r_1 \leq r \leq r_2) \\ h_1, & (r_2 \leq r \leq r_3) \end{cases} \quad (1)$$

The proposed 2D ABH-DVA is to be attached to a primary structure, exemplified by a plate, using either glue or a bolt, as shown in Fig 2. Since it is an add-on device, rather than an embedded indentation into the primary structure, it does not jeopardize the stiffness or the mechanical strength of the primary structure.

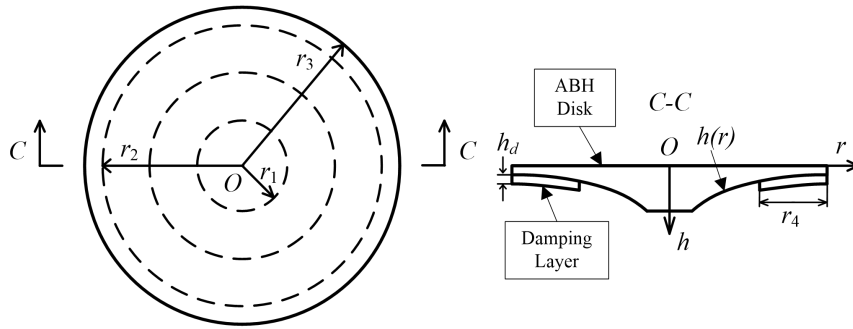


Fig.1. Schematic of a 2D circular ABH-DVA

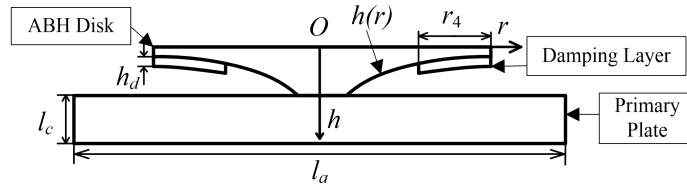


Fig.2. Synthesis system

To test the efficacy of the proposed device for vibration suppression and to understand the underlying physical mechanisms, FE simulations using Abaqus are carried out. The 3D FE model comprises a rectangular plate with free boundaries, with a lateral dimension of  $l_a$  by  $l_b$  and a thickness  $l_c$ , as the primary structure and a 2D ABH-DVA, as shown in Fig.2. The material and geometrical parameters of the combined system are tabulated in Tables 1 and 2, respectively. Both the primary plate and the ABH disk are made of aluminum, and the damping material is butyl rubber. The added mass of the ABH-DVA is 0.0529 kg (4.52% of the primary plate). To warrant a truthful description of the vibration details near the tip of the ABH-DVA and computational accuracy, the mesh size is set to ensure more than ten elements per wavelength. The model is discretized using C3D20R solid elements. To accommodate

the geometrical changes in the ABH region, the grid is divided in a non-uniform way, and the structure and additional damping layer are guaranteed to share common nodes at the interface.

Table 1 Material parameters

	Aluminum	Damping material
Young's modulus (MPa)	70000	200
Poisson's ratio	0.346	0.45
Density (kg m <sup>-3</sup> )	2710	1850
Material loss factor	0.001	0.1

Table 2 Structural geometric parameters

Parameters	Value
$l_a$	300 mm
$l_b$	240 mm
$l_c$	6 mm
$\varepsilon$	0.00112
$m$	2
$r_1$	5 mm
$r_2$	55 mm
$r_3$	61 mm
$h_0$	3 mm
$h_1$	0.2 mm
$h_d$	2 mm
$r_4$	30 mm

### 3. FE simulation analyses on vibration suppression and system coupling

#### 3.1 Vibration reduction of the plate with 2D ABH-DVA

The frequency response of the plate with and without the 2D ABH-DVA under an external force excitation is first investigated using the above FEM model. Placing the origin of the coordinate system at the center of the plate, as shown in Fig. 3, a transverse excitation force of 1 N in amplitude is applied at (100, 50) mm over the plate. The 2D ABH-DVA is rigidly connected to the primary structure at (-120, -90) mm. Modal analysis shows 26 flexural modes in the primary structure and 37 in the

2D ABH-DVA within the frequency range of interest (10 Hz to 5000 Hz). The modal superposition method was used to calculate the steady-state dynamic response of the structure for evaluation of the vibration suppression performance.

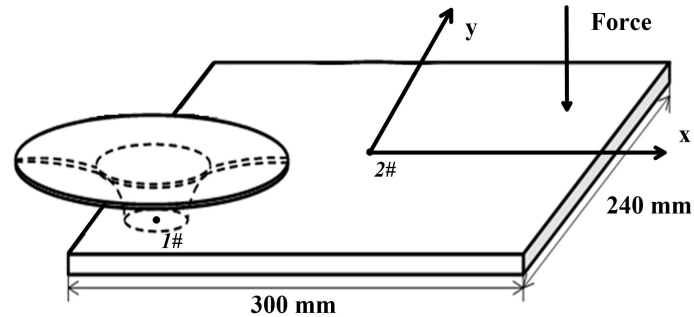


Fig.3. Sketch of the 2D ABH-DVA installed on a uniform plate

The driving point mobility is calculated with and without the ABH-DVA with results shown in Fig. 4. It can be seen that the deployment of the add-on ABH-DVA triggers obvious broadband vibration suppression of the host structure without particular parameter tuning in its design. Remarkable vibration suppression can be observed for some modes, such as those at 345 Hz, 1016 Hz and 2946 Hz, whilst less obvious effect is achieved for others, as shown in Fig. 4. Further inspection of the response curve suggests two main vibration suppression phenomena: the dynamic interaction (conventional DVA effect) evidenced by the typical peak splitting phenomenon; and damping enhancement (energy dissipation) as reflected by the reduction in some resonance peaks without splitting, in agreement with previous observations made in 1D ABH-RBD cases [22]. Different from the previous work, however, the presently proposed device seems to be able to cope with a large number of structural modes, which understandably should feature bi-directional deformation features. It is also understandable that the occurrence of the aforementioned phenomena would both rely on an effective dynamic coupling between the primary structure and the add-on ABH-DVA, which calls for further analyses which will be reported in the later section.

It is relevant to note that the aforementioned vibration reduction was checked to be caused by the ABH effects of the DVA. Numerical simulations show that a uniform disk with the same mass (through adjusting its thickness) and damping arrangement as the ABH-DVA could not produce the effects observed above. In order to ensure the

simplicity of the paper, the simulation results are not shown here, but only submitted as a supplementary material. Despite some noticeable changes on the host structure, no systematic vibration reduction could be achieved in the absence of the ABH feature. This is also consistent with the analyses in 1D cases [22, 24].

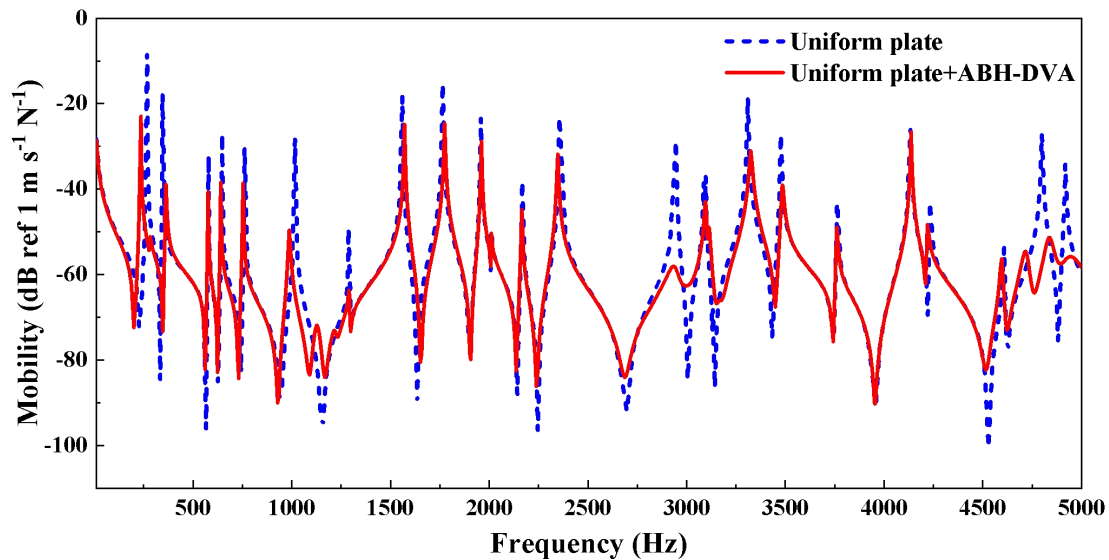


Fig.4. Comparisons of the driving point mobility of the primary plate with and without 2D ABH-DVA

### 3.2 Dynamic coupling analysis

In order to better understand the dynamic coupling characteristics between the two structural components and explain the observed phenomena, a substructuring formation is established followed by a coupling analysis. The analyses intend to show the structural interaction between the host structure and the ABH-DVA within some particular frequency ranges. As such, the model, along with the simplifications made and the way the model is to be used, should be understood in this particular context. Therefore, the formulation is not to be used as a predictive model for broadband system response calculation, which by the way, is accomplished using the aforementioned FE model with substructuring.

For convenience, only the out-of-plane displacement of the primary structure and auxiliary structure (2D ABH-DVA) are considered. Before they are coupled together, the discretized dynamic equation of each sub-system can be encapsulated in the

following discretized form:

$$\mathbf{M}_s \ddot{\mathbf{w}}_s + \mathbf{C}_s \dot{\mathbf{w}}_s + \mathbf{K}_s \mathbf{w}_s = \mathbf{F} \quad (2)$$

$$\mathbf{M}_A \ddot{\mathbf{w}}_A + \mathbf{C}_A \dot{\mathbf{w}}_A + \mathbf{K}_A \mathbf{w}_A = 0 \quad (3)$$

where  $\mathbf{M}_s$ ,  $\mathbf{C}_s$  and  $\mathbf{K}_s$  are the mass, damping and stiffness matrices for the primary structure respectively, and  $\mathbf{M}_A$ ,  $\mathbf{C}_A$  and  $\mathbf{K}_A$  are those for the add-on structure;  $\mathbf{w}_s$  and  $\mathbf{w}_A$  are the vibration displacement of the primary structure and the add-on structure respectively;  $\mathbf{F}$  is the excitation force on the primary structure.

Using the modal superposition method after modal mass normalization, Eqs. (2) and (3) can be cast into the following form in the principal modal coordinate system:

$$\mathbf{I} \ddot{\mathbf{q}}_s + [2\omega_s \zeta_s] \dot{\mathbf{q}}_s + [\omega_s^2] \mathbf{q}_s = \mathbf{F}_m \quad (4)$$

$$\mathbf{I} \ddot{\mathbf{q}}_A + [2\omega_A \zeta_A] \dot{\mathbf{q}}_A + [\omega_A^2] \mathbf{q}_A = 0 \quad (5)$$

where  $\mathbf{I}$  is the unit matrix;  $[2\omega_s \zeta_s]$  a diagonal matrix with its  $i$ th diagonal element equal to  $2\omega_{si} \zeta_s$  with  $\omega_{si}$  and  $\zeta_s$  being the natural frequencies and the corresponding modal damping ratios of the plate.  $[\omega_s^2]$  is another diagonal matrix containing  $\omega_{si}^2$  as diagonal elements. Replacing sub-index  $s$  by  $A$  leads to the counterparts of these quantities in the absorber.  $\mathbf{q}_s$  and  $\mathbf{q}_A$  are the modal coordinates of the primary structure and add-on structure respectively.

Now imposing the coupling, the ABH-DVA is bonded to the primary structure within a circular interfacial area enclosed by a radius  $r=r_1$  (Fig. 2). Assuming a small interfacial area with respect to the bending wavelength, the out-of-plane motion within the contact area can be described by a translational displacement and a rotational angle. To illustrate the process, consider only the translational motion of the ABH-DVA at a single joint node between the two substructures. The displacement of the main structure at the same joint node can be expressed as:

$$w_{sn} = \mathbf{G} \Phi_s \mathbf{q}_s \quad (6)$$

where  $\Phi_s$  is the modal matrix of the primary structure,  $\mathbf{G} = \{0 \dots 0, 1, 0 \dots 0\}$  is row vector with components of zeros except the one corresponding to the joint node.

The ABH-DVA, once added on the primary structure, is excited by the plate motion. Its displacement writes:

$$\mathbf{w}_A = \mathbf{\Phi}_A \mathbf{q}_A + \gamma \{1\} w_{sn} \quad (7)$$

where  $\mathbf{\Phi}_A$  is modal matrix of the ABH-DVA,  $\{1\}$  is a column vector with all the components equal to 1.  $\gamma$  factor is used to ensure the displacement continuity between the base structure and the DVA. This is necessary because the mode vectors of the ABH-DVA are calculated under unconstrained conditions.

Substitution of Eqs. (7) and (6) into Eq. (5) gives the modal equation of the ABH-DVA as:

$$\mathbf{I}\ddot{\mathbf{q}}_A + [2\omega_A \zeta_A] \dot{\mathbf{q}}_A + [\omega_A^2] \mathbf{q}_A = -\gamma \mathbf{\Phi}_A^T \mathbf{M}_A \{1\} \mathbf{G} \mathbf{\Phi}_s \ddot{\mathbf{q}}_s. \quad (8)$$

Obviously the right-hand-side term which contains the modal coordinates of the primary structure, physically corresponds to the excitation force imposed by the primary structure on the DVA.

The same coupling force is also applied to the primary structure. Therefore, the dynamical modal equation (5) of the primary structure can be expressed as:

$$\mathbf{I}\ddot{\mathbf{q}}_s + [2\omega_s \zeta_s] \dot{\mathbf{q}}_s + [\omega_s^2] \mathbf{q}_s = \mathbf{F}_m - \gamma \mathbf{\Phi}_s^T \mathbf{G}^T \{1\}^T \mathbf{M}_A \mathbf{\Phi}_A \ddot{\mathbf{q}}_A. \quad (9)$$

Should it be necessary, the natural frequency and modal vectors of the coupled system can be obtained by simultaneously solving these two coupled equations (8) and (9), reflecting the two-way interaction effect between the two structural components. Instead, the above equations will be used to explain the modal interaction behavior between the two structural components at relatively low and narrow band frequency. Therefore, we focus on the resonant response of the primary structure when one of its modes dominates. Considering the orthogonality among the modes of the 2D ABH-DVA before coupling and the linearity of the system, the influence of each ABH-DVA mode can also be scrutinized separately upon some implication of the model. This allows the problem to be simplified. Without compromising the general coupling principle, some particular mode pairs are selected in order to highlight their coupling characteristics.

Assuming that  $i$ th mode in the primary structure and the  $j$ th mode in the add-on DVA dominate the system response under a modal excitation force  $F_{mi}$ . The equations of dynamic motion (Eqs. (8) and (9)) become:

$$\ddot{q}_{si} + \alpha_{ij} \ddot{q}_{Aj} + 2\omega_{si} \zeta_s \dot{q}_{si} + \omega_{si}^2 q_{si} = F_{mi}, \quad (10)$$

$$\ddot{q}_{Aj} + \alpha_{ij}\ddot{q}_{si} + 2\omega_{Aj}\zeta_A\dot{q}_{Aj} + \omega_{Aj}^2q_{Aj} = 0, \quad (11)$$

where  $\alpha_{ij}$  is an important parameter to quantify the coupling strength between the two structures, referred to as the modal coupling coefficient. In accordance to Eq. (9),  $\alpha_{ij}$  is mathematically defined as:

$$\alpha_{ij} = \gamma \Phi_{Ai}^T \mathbf{M}_A \{1\} \mathbf{G} \Phi_{sj} = \gamma \Phi_{Ai}^T \mathbf{M}_A \cdot \mathbf{G} \Phi_{sj}. \quad (12)$$

It is clear that,  $\alpha_{ij}$  not only depends on the two modes involved including their respective mode shapes, but also the location of the ABH-DVA.

The influence of coupling coefficient on vibration suppression effect is analyzed and discussed in the following for two cases: first, the modal frequency of the primary plate is close to that of the add-on structure; second, the difference between the two is relatively large.

### Dynamic interaction

When the excitation frequency  $\omega$  is close to both  $\omega_{si}$  and  $\omega_{Aj}$ , one has

$$\begin{bmatrix} \omega_{si}^2 - \omega^2 + j2\zeta_s\omega_{si}\omega & -\alpha_{ij}\omega^2 \\ -\alpha_{ij}\omega^2 & \omega_{Aj}^2 - \omega^2 + j2\zeta_A\omega_{Aj}\omega \end{bmatrix} \begin{Bmatrix} \tilde{q}_{si} \\ \tilde{q}_{Aj} \end{Bmatrix} = \begin{Bmatrix} \bar{F}_{mi} \\ 0 \end{Bmatrix} \quad (13)$$

where  $\bar{F}_{mi}$ ,  $\tilde{q}_{si}$  and  $\tilde{q}_{Aj}$  denote the amplitude of  $F_{mi}$ ,  $q_{si}$  and  $q_{Aj}$  respectively. Solution of Eq. (13) gives

$$\tilde{q}_{si} = \frac{\omega_{Aj}^2 - \omega^2 + j2\zeta_A\omega_{Aj}\omega}{\Delta} \bar{F}_{mi} \quad (14)$$

where

$$\Delta = (\omega_{si}^2 - \omega^2 + j2\zeta_s\omega_{si}\omega)(\omega_{Aj}^2 - \omega^2 + j2\zeta_A\omega_{Aj}\omega) - \alpha_{ij}^2\omega^4. \quad (15)$$

Obviously in the approximated 2DOF system, the add-on structure acts as a dynamic vibration absorber on the primary structure. As such, the original resonance peak of the primary structure is expected to split into two, the frequencies of which are the eigenvalue solution of Eq. (15) and the height depends on  $\zeta_A$ ,  $\omega_{Aj}$  and  $\omega_{si}$ . When  $\omega_{Aj} = \omega_{si}$ , defining

$$\Omega = \omega / \omega_{si} \quad (16)$$

the two resonance frequencies of the undamped counterpart of Eq. (15) are

$$\Omega_{1,2}^2 = \frac{1}{1 \pm \alpha_{ij}}. \quad (17)$$

The complex amplitude of modal coordinates of the primary structure with the add-on structure at these two frequencies can be obtained as:

$$q_{si} = \frac{1 - \Omega^2 + j2\zeta_A \Omega}{-4\zeta_s \zeta_A \Omega^2 + j2(\zeta_s + \zeta_A)(1 - \Omega^2)\Omega} \cdot \frac{F_{mi}}{\omega_{si}^2} \quad (18)$$

with  $\Omega = \Omega_1$  or  $\Omega = \Omega_2$ .

As a special case without ABH-DVA,  $\alpha_{ij} = 0$  and in that case,  $\Omega_1 = \Omega_2$ . The amplitude of modal coordinate of the primary structure is

$$\bar{q}_{si} = \frac{1}{2\zeta_s} \cdot \frac{F_{mi}}{\omega_{si}^2}. \quad (19)$$

Obviously, the ratio between the modal displacement amplitude of the primary structure with and without add-on structure can be used to evaluate the vibration suppression effect of the add-on structure, defined as

$$A = \frac{\tilde{q}_{si}}{\bar{q}_{si}} = \frac{(1 - \Omega^2 + j2\zeta_A \Omega)2\zeta_s}{-4\zeta_s \zeta_A \Omega^2 + j2(\zeta_s + \zeta_A)(1 - \Omega^2)\Omega} \Bigg|_{\Omega=\Omega_{1,2}}, \quad (20)$$

where  $|A|$  is a function of  $\Omega_{1,2}$ , which, in turn, is a function of  $\alpha_{ij}$ . The relationship between  $|A|$  and  $\alpha_{ij}$  with different  $\zeta_A$  when  $\zeta_s=0.001$  and  $\Omega = \Omega_1$  is plotted in Fig. 5(a), which shows that the larger the coupling coefficient  $\alpha_{ij}$ , the better the control effect. However, even for a small coupling coefficient, an appreciable control effect can still be obtained. Meanwhile, the control effect is not significantly affected by the modal damping ratio of the ABH-DVA. Therefore, perfect vibration suppression is possible, as long as the primary structure and the ABH-DVA meet certain coupling conditions, as shown in Eq. (12).

### **Damping enhancement**

An ABH-DVA mode with  $\omega_{Aj}$ , which is significantly different from  $\omega_{si}$ , can be regarded as a damping contributor to the primary system. When the primary structure is excited around its resonance frequency  $\omega_{si}$ , that is,  $\Omega = \omega/\omega_{si} \approx 1$ , the response of the ABH-DVA can be expressed in the following form:

$$\tilde{q}_{Aj} = \frac{\alpha_{ij} \Omega^2}{\beta_{ij}^2 - \Omega^2 + j2\zeta_A \Omega \beta_{ij}} \cdot \tilde{q}_{si} \quad (21)$$

where  $\beta_{ij} = \omega_{Aj} / \omega_{si}$ . When  $\omega_{Aj} \gg \omega_{si}$ , then  $\beta_{ij} \gg 1$ . With  $\Omega \approx 1$ ,  $|\tilde{q}_{Aj}| \leq |\tilde{q}_{si}|$ , suggesting that the dynamic effect of the ABH-DVA on the primary structure is of secondary effect. On the contrary, when  $\omega_{Aj} \ll \omega_{si}$ ,  $\beta_{ij} \ll 1$ . By neglecting the second order term,  $\beta_{ij}^2$  in the denominator, one has:

$$\tilde{q}_{Aj} = -\frac{\alpha_{ij}}{1 - j2\zeta_A \beta_{ij} / \Omega} \cdot \tilde{q}_{si} \approx -\alpha_{ij} (1 + j2\zeta_A \beta_{ij} / \Omega) \tilde{q}_{si}. \quad (22)$$

Substitution of Eq. (22) into Eq. (10) gives

$$\left\{ [1 - \Omega^2 (1 - \alpha_{ij}^2)] + j2\Omega (\zeta_s + \alpha_{ij}^2 \beta_{ij} \zeta_A) \right\} \tilde{q}_{si} = \bar{F}_{mi} / \omega_{si}^2. \quad (23)$$

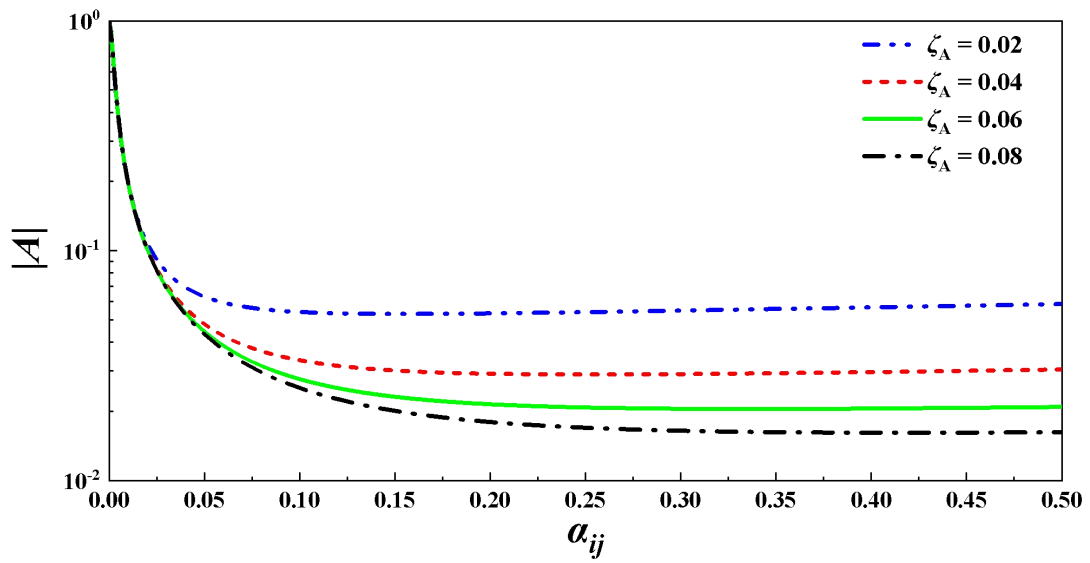
Obviously, this gives an equivalent damping ratio, *i.e.*  $\zeta_s + \alpha_{ij}^2 \beta_{ij} \zeta_A$ , denoted by  $\zeta_c$

$$\zeta_{ci} = \zeta_s + \alpha_{ij}^2 \beta_{ij} \zeta_A. \quad (24)$$

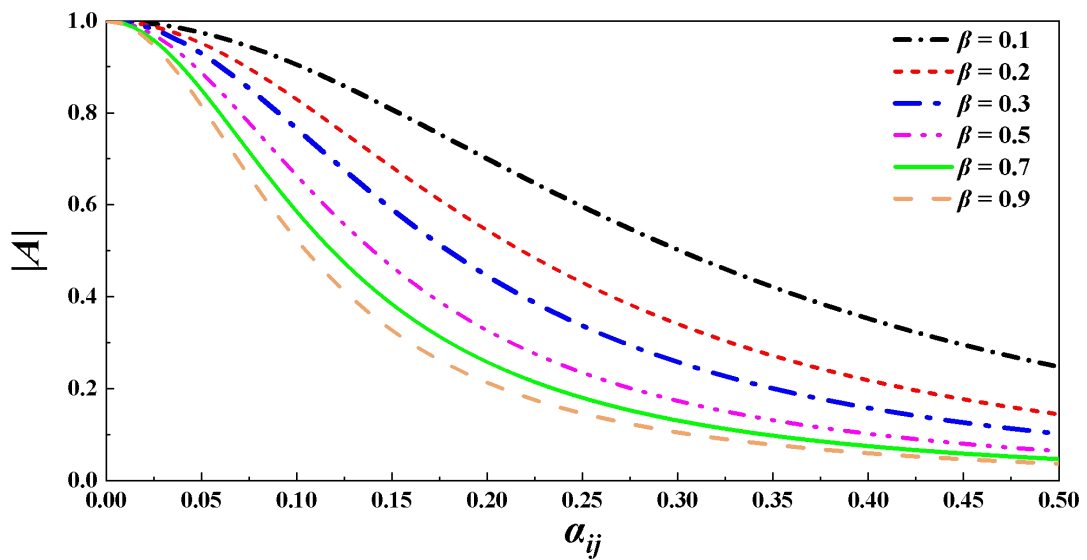
The above expression indicates that a low-frequency mode of the ABH-DVA can add damping to a strongly coupled mode of the primary structure with a higher resonance frequency. Using Eq. (20), one has:

$$A = \frac{\tilde{q}_{si}}{\bar{q}_{si}} = \frac{2\zeta_s}{j2\Omega (\zeta_s + \alpha_{ij}^2 \beta_{ij} \zeta_A)} \Big|_{\Omega = \sqrt{1/(1-\alpha_{ij}^2)}}. \quad (25)$$

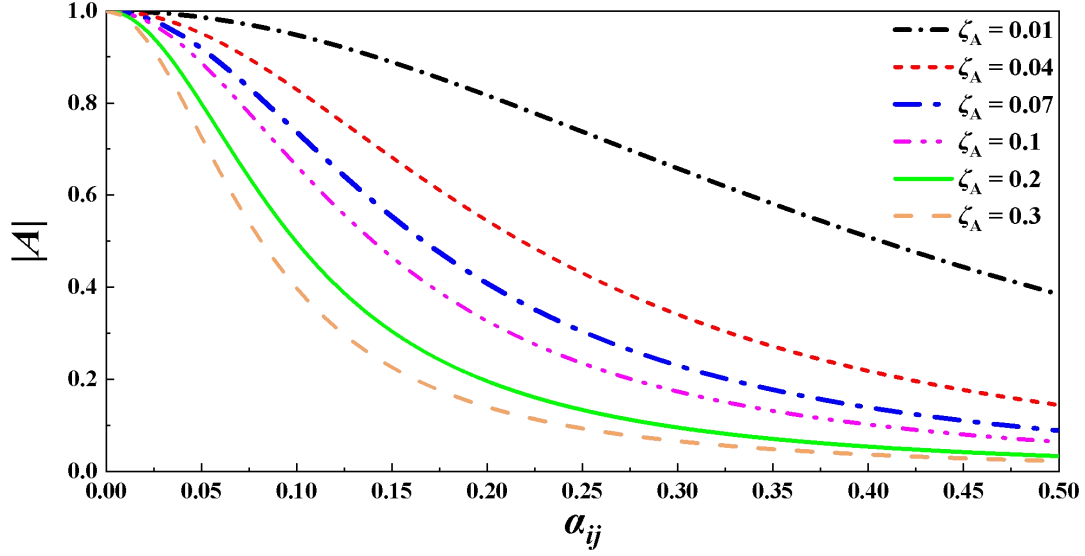
The relationship between  $|A|$  and  $\alpha_{ij}$  with  $\zeta_A = 0.1$ ,  $\zeta_s = 0.001$  and varying  $\beta_{ij}$  from 0.1 and 0.9 is plotted in Fig.5 (b). It follows that, for the same modal damping ratio of the ABH-DVA, the larger the frequency ratio is, the better the control effect is, *i.e.* better control effect for those modes whose natural frequencies are closer to that of the ABH-DVA. From a different perspective,  $|A| - \alpha_{ij}$  relationship with  $\beta_{ij} = 0.5$ ,  $\zeta_s = 0.001$  and varying  $\zeta_A$  from 0.01 and 0.3 is plotted in Fig. 5(c). It can be seen that, although the control effect is less pronounced than that of the dynamic interaction under the same coupling coefficient, appreciable control can still be obtained by increasing either  $\zeta_A$  or the coupling coefficient. Therefore, a damping enhancement in the primary structure can be obtained by increasing the modal damping ratio of the add-on structure when the resonance frequencies of primary structure are higher than those of the ABH-DVA.



(a)  $\Omega = \Omega_1$  and  $\zeta_s = 0.001$



(b)  $\zeta_A = 0.1$  and  $\zeta_s = 0.001$



(c)  $\beta_{ij} = 0.5$  and  $\zeta_s = 0.001$

Fig.5. Relationship between normalized control effect and coupling coefficient

### 3.3 Control mechanisms and the parametric influence on control performance

Based on the above analysis tool, dynamic features related to the proposed ABH-DVA as well as its coupling with the host plate are scrutinized in this section. This allows one to understand how the aforementioned mechanisms are materialized in the current context.

#### 3.3.1 Dynamic coupling characteristics of the 2D ABH-DVA

Eqs. (20) and (25) and the results of Fig. 5 suggest that the vibration suppression effect is directly related to the coupling coefficient  $\alpha_{ij}$ , no matter which mechanism dominates the process. In order to gain insights into the factors that influence  $\alpha_{ij}$ , discussions are made on the physical meaning of the two parts in Eq. (12),  $\Phi_{Ai}^T \mathbf{M}_A \{1\}$  and  $\mathbf{G}\Phi_{sj}$ , both of which are real numbers. For the convenience of discussion, Eq. (12) is rewritten as:

$$\alpha_{ij} = \gamma \cdot \alpha_{ij}^{(1)} \cdot \alpha_{ij}^{(2)} \quad (26)$$

where

$$\alpha_{ij}^{(1)} = \Phi_{Ai}^T \mathbf{M}_A \{1\} = \Phi_{Ai}^T \mathbf{M}_A, \quad \alpha_{ij}^{(2)} = \mathbf{G}\Phi_{sj}. \quad (27)$$

According to the definition of the vector  $\mathbf{G}$ ,  $\alpha_{ij}^{(2)}$  is a specific component of the vector  $\Phi_{sj}$ . The absolute value of  $\alpha_{ij}^{(2)}$  reaches maximum when the ABH-DVA is installed at the peak of the mode shape of the primary structure. The term  $\alpha_{ij}^{(1)}$  is the mass-weighted summation of the components of modal vectors of the add-on structure. Its value depends on the mode shape of the ABH-DVA.

### **Influence of mode shape on the coupling coefficient**

Some typical modal shapes of the 2D ABH-DVA are shown in Fig.6, in which the notation  $RmCn$  denotes an ABH-DVA mode with a radial order  $m$  and a circumferential order  $n$ . Due to the axisymmetric geometry of the circular ABH-DVA, its natural modes corresponding to the lateral vibration can be expressed as

$$\Phi_{Amn}(r, \theta) = W_m(r) \cos(n\theta). \quad (28)$$

Any combination of  $(m, n)$  corresponds to an  $i$  in the index of  $\alpha_{ij}$ . As examples, three circumferential 5th-order modes are shown in Fig.7. The continuous counterpart of  $\alpha_{ij}^{(1)}$  in Eq. (27) is

$$\alpha_{ij}^{(1)} = \Phi_{Ai}^T \mathbf{M}_A = \iint W_m(r) \cos(n\theta) \rho r dr d\theta \quad (29)$$

where  $\rho$  is the density of the ABH-DVA. It is obvious from Eq. (29) that  $\alpha_{ij}^{(1)}$  equals zero when  $n \geq 1$ . Therefore, only the fundamental circumferential modes with  $n=0$  are coupled with the primary structure. It follows that, only a few modes of 2D ABH-DVA are strongly coupled with the primary structure although there are much greater number of modes in the 2D ABH-DVA than the primary structure.

The modal damping ratios of the system and its constituents are shown in Fig. 8. The resonance frequencies and modal damping ratios of the modes below 1600 Hz are listed in Table 3. The damping ratios of all the modes of the primary structure are 0.0005, which is half the material loss factor of the primary structure. The triangle ones denote the modal damping ratios of ABH-DVA itself, which are much greater than those of the primary structure due to the combination of the ABH effect and the damping layer [4, 23]. It is also obvious that the modes of the ABH-DVA can be roughly classified into three groups, as labeled in Fig.8. Further inspection of their

mode shapes shows that the modes in each group share the same radial order, corresponding to the radially 1st, 2nd, and 3rd orders, respectively. Based on the above coupling analysis, only three modes, (1, 0), (2, 0) and (3, 0), can be coupled with the primary structure. The frequencies of the three modes are 302 Hz, 1210 Hz and 2952 Hz, respectively. This explains why the dynamic interaction effect is only observed around 300 Hz, 1200 Hz and 2900 Hz in Fig.4.

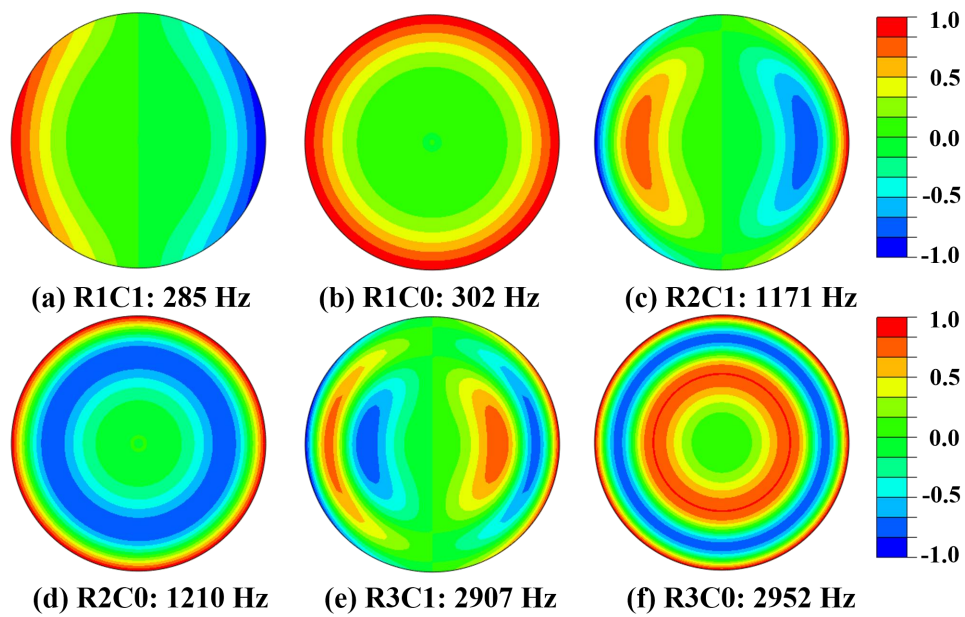


Fig. 6 Modal shapes of 2D ABH-DVA coupled with the primary plate

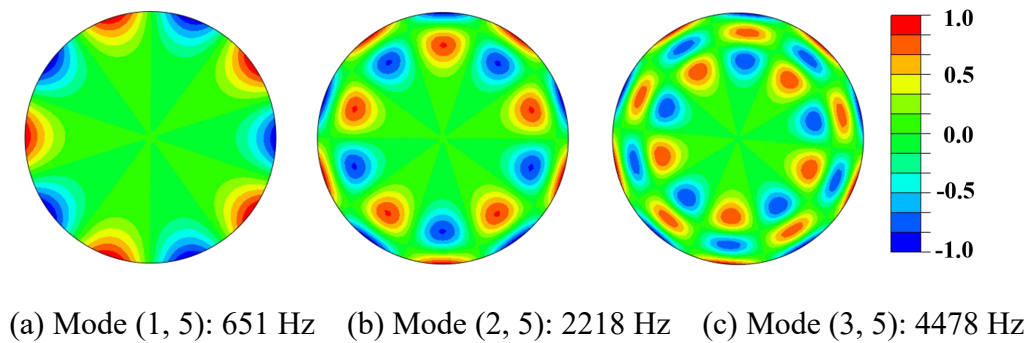


Fig. 7 Radial modes of first, second, and third order of the ABH structure

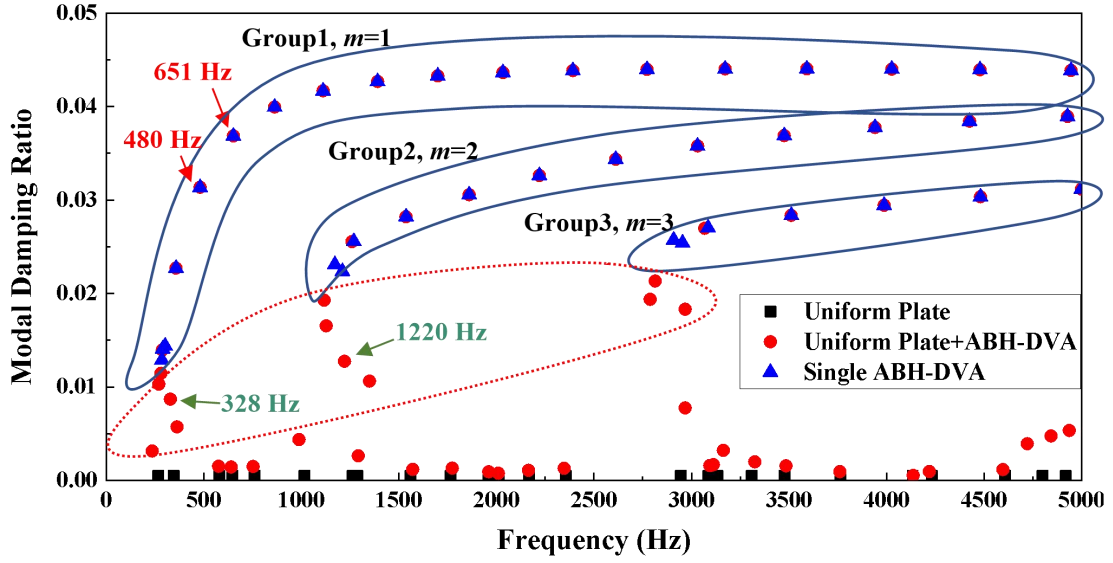


Fig.8. Modal damping ratios of the combined system and different components

The ABH-DVA has 37 modes in the frequency range from 10 Hz to 5000 Hz, much more than the number of modes in the primary structure. Although the rich dynamic of the ABH-DVA can theoretically increase the chance to match the modal frequency of the primary structure, many of them however cannot be efficiently coupled with the primary structure in practice. Modal frequencies and modal damping ratios of different structures in the frequency range of 0-1600 Hz are tabulated in Table 3. The modes of 2D ABH-DVA with  $n=0$  and  $n=1$  are shown in bold and italic. The results in Fig.8 and Table 3 also clearly show that all the modes  $(m, n)$  of the 2D ABH-DVA with  $n \geq 2$  are almost completely decoupled with the primary structure, since they all preserve their modal features even after the coupling. Taking mode (1, 4) of the 2D ABH-DVA as an example, the uncoupled natural frequency (480.37 Hz) and the damping ratios (0.0314) basically remain intact in the combined system (480.35 Hz and 0.0313, respectively) as shown in Table 3. Their modes shapes are shown in Figure 9.

Another example is mode (1, 5) of the 2D ABH-DVA shown in Fig.10(a) at 651.16 Hz with a damping ratio of 0.0369. In light of Eq. (29), this mode cannot be coupled with the primary structure. Although there is a mode in the primary structure with very close resonance frequency at 647.46 Hz, shown in Fig.10(b), these two modes indeed are not coupled and there is no dynamic interaction effect. The frequency of the mode in the combined system corresponding to mode (1, 5) of ABH-DVA, as shown in Fig.10(d), is 651.13 Hz and its damping ratio is 0.0369,

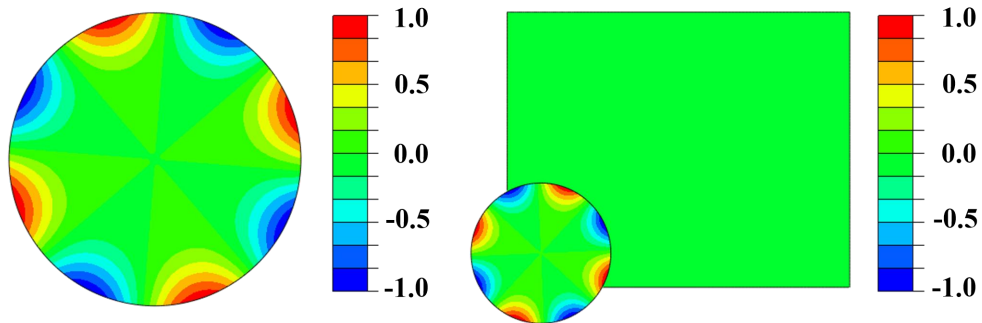
almost the same as that of the ABH-DVA itself. The mode in the combined system corresponding to the original mode of the primary structure, as shown in Fig.10(c), has a frequency of 640.10 Hz, which is slight lower than the frequency of the original mode because the ABH-DVA can be approximated as a lumped mass in this case. Its modal damping ratio is slightly increased from 0.0005 to 0.0014, which can be affected by other frequencies as explained by Eq. (25).

Table 3 Modal frequencies and modal damping ratios of different structures

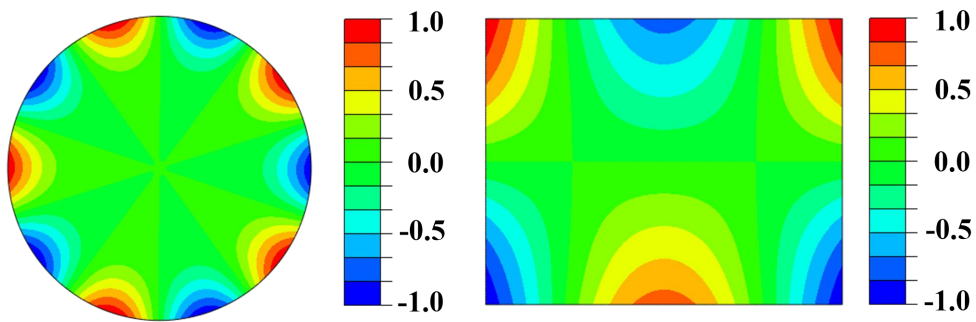
Uniform Plate		ABH-DVA		Synthetic system	
Frequency (Hz)	Modal damping ratio	Frequency (Hz)	Modal damping ratio	Frequency (Hz)	Modal damping ratio
267.44	0.0005	<b>285.12</b>	0.0129	235.84	0.0031
345.42	0.0005	289.21	0.0141	269.62	0.0103
578.51	0.0005	<b>301.65</b>	0.0144	280.45	0.0115
647.46	0.0005	357.14	0.0227	287.62	0.0140
761.05	0.0005	480.37	0.0314	328.41	0.0087
1016.07	0.0005	651.16	0.0367	357.05	0.0227
1262.56	0.0005	862.88	0.0400	362.61	0.0057
1286.87	0.0005	1110.30	0.0417	480.35	0.0314
1560.01	0.0005	<b>1171.34</b>	0.0231	576.04	0.0015
		<b>1209.64</b>	0.0224	640.10	0.0014
		1268.37	0.0256	651.13	0.0369
		1389.54	0.0427	752.77	0.0015
		1535.70	0.0282	862.85	0.0400
				987.40	0.0044
				1110.28	0.0417
				1115.59	0.0193
				1127.25	0.0165
				1220.22	0.0128
				1259.57	0.0256
				1291.82	0.0026
				1350.10	0.0106
				1389.51	0.0427
				1535.18	0.0282
				1571.10	0.0012

It should be noted that, the qualitative modal coupling analysis based on translational continuity between the ABH-DVA and the plate, ignores the rotational motion of the connecting area. Should this effect be taken into account, additional

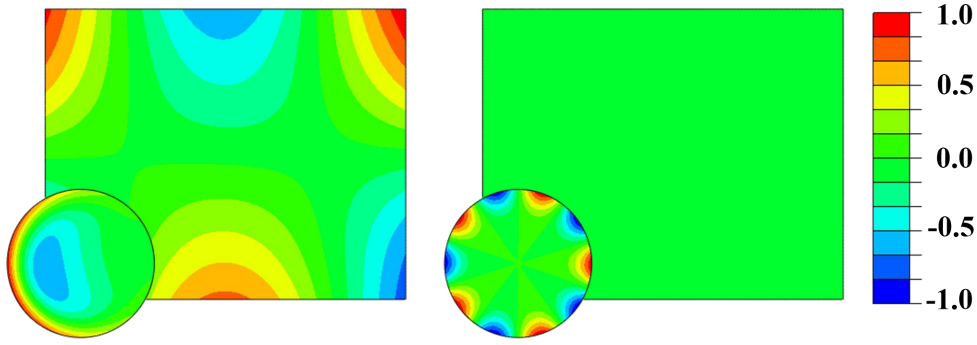
coupling path can be created. This is demonstrated by examining three modes (1, 1), (2, 1) and (3, 1), with a frequency of 285.12 Hz, 1171.34 Hz and 2906.7 Hz, respectively. The commonality among the three modes is that, according to the mode shapes shown in Fig. 6, they share the same circumferential deformation denoted by  $(m, 1)$  ( $m=1,2,3$ ). Indeed, they are coupled with primary structure through rotation, which can be observed in the FE simulation results because both the lateral motion and the rotational motion were considered in the FE simulations. Nevertheless, even with the addition of these modes, effective coupling can only be possible between the plate and a small number of ABH-DVA modes, due to the axis-symmetrical geometry of the device.



(a) ABH-DVA: 480.37 Hz      (b) Uniform plate-ABH-DVA system: 480.35 Hz  
 Fig.9. Modal shapes at 480 Hz of single ABH-DVA and synthetic system



(a) ABH-DVA: 651.16 Hz      (b) Uniform plate: 647.46 Hz



Uniform plate-ABH-DVA system: (c) 640.10 Hz, (d) 651.13 Hz

Fig.10. Modal shapes of different systems near 647 Hz

From the above discussions, it is obvious that the vibration modes of the combined system can be divided into three categories: the primary structure-dominant modes, the ABH-DVA dominant modes and coupled modes. The ABH-DVA dominant modes have little influence on the primary structure and are not visible in the frequency responses in Fig. 4. All the coupled modes are the results of modal combination of the primary structure and 2D ABH-DVA, as discussed in Section 3.2. In the present case, these modes appear around 320 Hz, 1200 Hz and 2900 Hz. They exhibit strong dynamic interaction as shown in Fig.8. The primary structure-dominant modes are weakly influenced by the modes of the 2D ABH-DVA and their damping ratios are slightly increased, as indicated by Eq. (25), which will be discussed in the following.

### **Influence of the ABH-DVA installation position on coupling coefficient**

As shown in Eqs. (26) and (27), the installation position of the ABH-DVA also affects the coupling coefficient. If the modal function of the  $j$ th mode in the continuous form is  $\phi_{sj}(x, y)$ , the continuous counterpart of  $\alpha_{ij}^{(2)}$  in Eq. (27) is

$$\alpha_{ij}^{(2)} = \mathbf{G}\Phi_{sj} = \iint \phi_{sj}(x, y) \delta(x - x_A, y - y_A) dx dy = \phi_{sj}(x_A, y_A) \quad (30)$$

where  $\delta(x, y)$  is a two-dimensional Dirac  $\delta$  function and  $(x_A, y_A)$  is the installation coordinate of the 2D ABH-DVA on the primary structure. It is obvious that the 2D ABH-DVA should be installed at the maximum vibration displacement area of the primary structure to maximize the coupling coefficient.

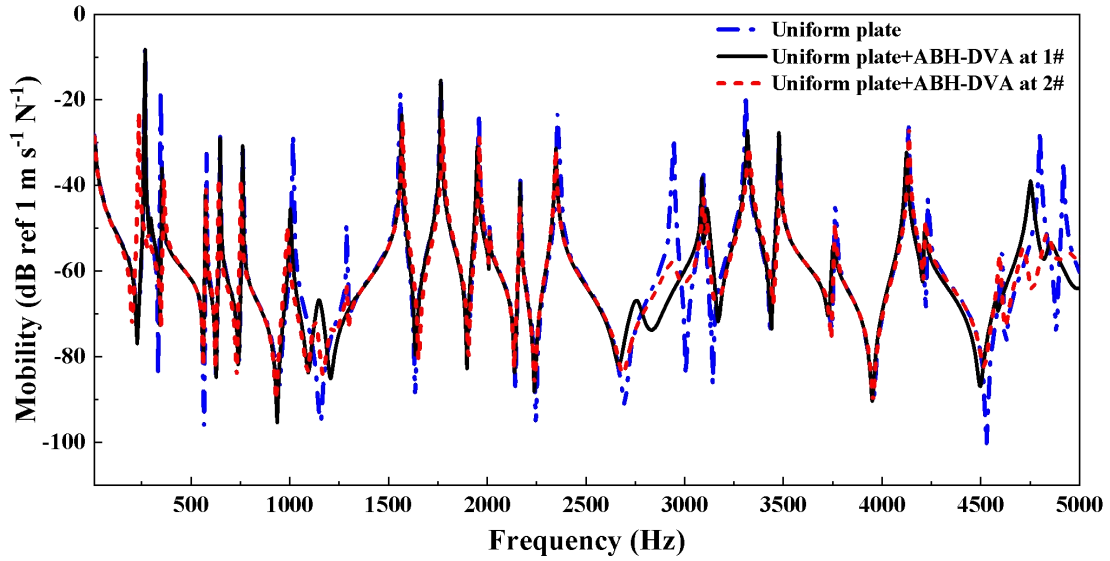
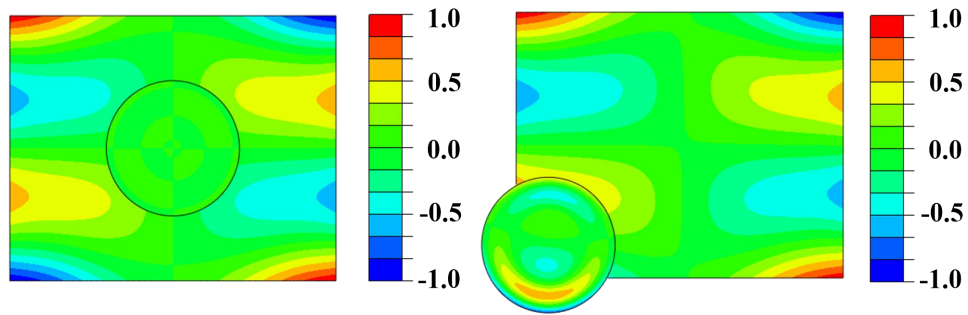


Fig.11. Driving point mobility at different positions



(a) 1#

(b) 2#

Fig.12. Modes at 1765 Hz of the combined system with different mounting positions

To illustrate this effect, the frequency response of the primary structure is calculated when the 2D ABH-DVA is installed at the center of the plate at (0, 0) mm. Comparisons are made with the nominal case at (-120, -90) mm in Fig.11, which shows a reduced vibration suppression effect for some major peaks, exemplified by 1765 Hz. The modal deformation at 1765 Hz, shown in Fig. 12, confirms that the mode has a nodal line cross the middle of the plate, thus neutralizing the possible coupling with the ABH-DVA.

### 3.3.2 Damping enhancement by the 2D ABH-DVA

As shown in Eq. (24), the damping effect of the strongly coupled ABH-DVA modes can contribute to the modal damping ratio of the primary structure even the

resonance frequencies of ABH-DVA modes are not close to those of the primary structure modes. The modes of the ABH-DVA, that are strongly coupled with the primary structure in the frequency range up to 5 kHz, are modes R1C1, R1C0, R2C1, R2C0, R3C1, and R3C0. Their frequencies and mode shapes are shown in Fig. 6. According to Eq. (24), the damping enhancement is only effective when  $\beta_{ij} < 1$  and the effect proportionally decreases with  $\beta_{ij}$ . It implies that R1C1 and R1C0 modes would contribute to the damping of all the coupled modes of the primary structure without dominant dynamic interaction effect above 300 Hz; whilst R2C1 and R2C0 to those modes above 1100 Hz and R3C1 and R3C0 to those modes above 2800 Hz. As an example, the modal damping ratio of mode  $i$  between 1100 Hz to 2800 Hz can be expressed in the following form

$$\begin{aligned}\zeta_{ci} &= \zeta_s + \sum_{\beta_{ij} < 1} \alpha_{ij}^2 \beta_{ij} \zeta_{Aj} \\ &= \zeta_s + \alpha_{i(1,1)}^2 \beta_{i(1,1)} \zeta_{A(1,1)} + \alpha_{i(1,0)}^2 \beta_{i(1,0)} \zeta_{A(1,0)} + \alpha_{i(2,1)}^2 \beta_{i(2,1)} \zeta_{A(2,1)} + \alpha_{i(2,0)}^2 \beta_{i(2,0)} \zeta_{A(2,0)}\end{aligned}, \quad (31)$$

where the index  $j$  has been replaced by  $(m, n)$ . Because the damping enhancement effect is proportional to  $\beta_{ij} = \omega_{si} / \omega_{Aj}$  and the modes R2C1 and R2C0 take greater value of  $\beta$ , these two modes have greater contribution to the damping ratios of the primary structure from 1100 Hz to 2800 Hz than the modes R1C1 and R1C0.

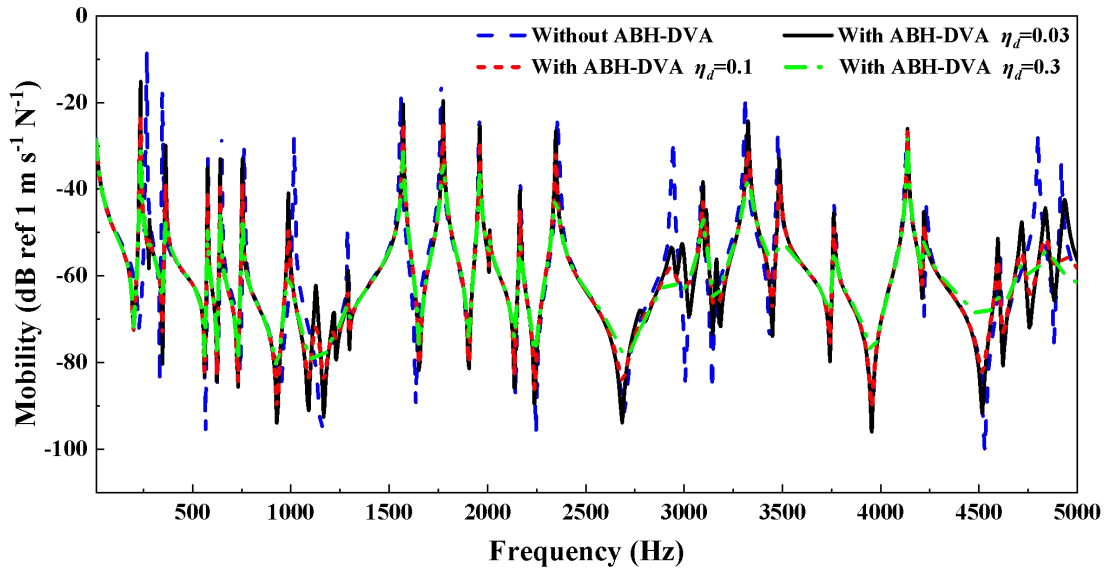
In the FEM simulations,  $\zeta_{Aj}$  is adjusted by changing the material loss factor of the damping layer pasted on the ABH disk, which is denoted by  $\eta_d$ . The driving point mobility curves and the modal damping ratio of the primary structure without and with the ABH-DVA with different  $\eta_d$  are shown in Fig. 13. Special attention is paid to the modes of the primary structure without dominant dynamic interaction effect. It can be seen that the damping ratio of almost all the modes in the primary structure is increased when  $\eta_d$  increases, except for a few modes which are not coupled with the ABH-DVA. For example, the mode at 4136 Hz is not affected because the installation location of the ABH-DVA is on the nodal line of this mode.

The linear FEM analysis used in this study stipulates that  $\zeta_{Aj} = k_{Aj} \eta_d$ , where  $k_{Aj}$  is the coefficient taking different value for different mode  $j$ . As an example, the relationship between the material loss factor  $\eta_d$  of the coating layers and the modal damping ratios  $\zeta_{Aj}$  of the mode R1C0 and R1C1 of the ABH-DVA is shown in Fig.

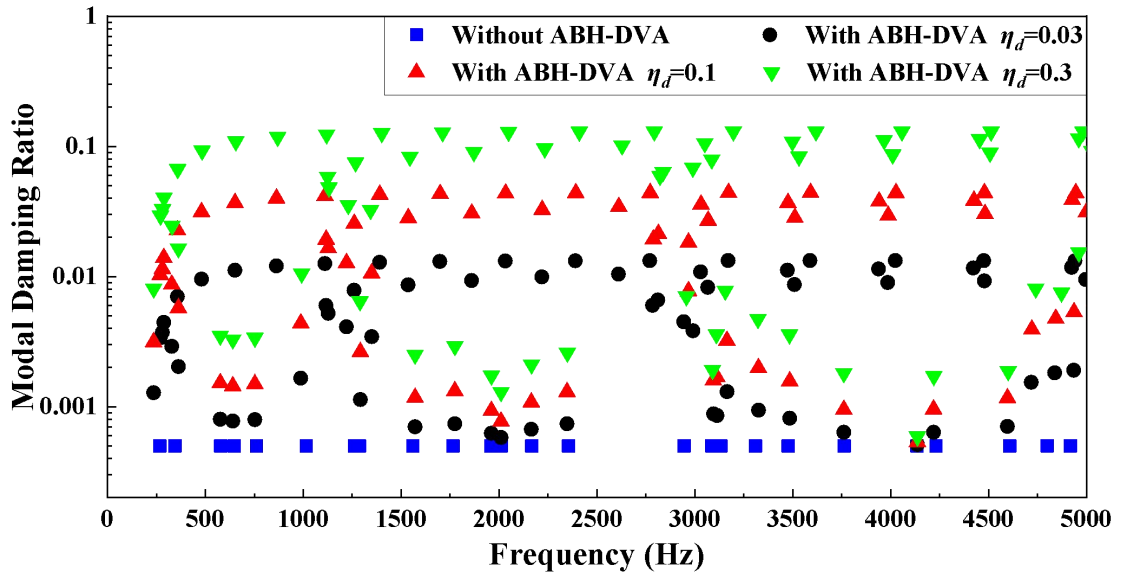
14, with slopes of 0.1404 and 0.1254 for the two modes respectively. When assigning  $\eta_d = 0$  to the damping material,  $\zeta_{A_j}$  is 0.0004, which is less than half the loss factor of the material of the ABH-DVA. Increasing  $\eta_d$  to 0.3,  $\zeta_{A_j}$  reaches 0.0425 for R1C0 and 0.0380 for R1C1. Due to the ABH effect, the modal damping ratio of the ABH-DVA,  $\zeta_{A_j}$ , can be greatly increased upon using a small amount of damping material. According to Eq. (31), the enhanced damping ratio of structural mode can be expressed as

$$\zeta_{ci} = \zeta_s + \left( \sum_{\beta_{ij} < 1} \alpha_{ij}^2 \beta_{ij} k_{A_j} \right) \eta_d. \quad (32)$$

As an example, the damping ratio and the driving point mobility of the mode at 640.1 Hz of the primary structure are calculated for different value of  $\eta_d$  and the results are plotted in Fig. 15. Interestingly enough,  $\zeta_{ci}$  and  $\eta_d$  shows a coherent and linear relationship and the slope is estimated as  $\alpha_{i(1,1)}^2 \beta_{i(1,1)} k_{A(1,1)} + \alpha_{i(1,0)}^2 \beta_{i(1,0)} k_{A(1,0)} = 0.0093$ . The driving point mobility of the modal response also decreases with the increase of  $\eta_d$ . When  $\eta_d$  is increased from 0.03 to 0.3, the modal vibration response at 640.1 Hz is reduced by as much as 12.43 dB, as a result of the enhanced damping contributed by the lower-order, strongly coupled and remotely spaced ABH-DVA modes.



(a) Driving point mobility of the primary structure



(b) Modal damping ratio of the primary structure

Fig.13. Driving point mobility and modal damping ratio of the primary structure without and with ABH-DVA considering different damping of the coating layers

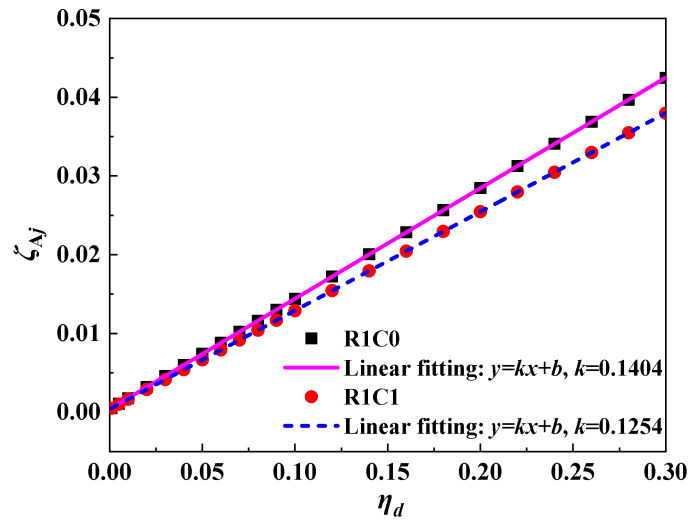
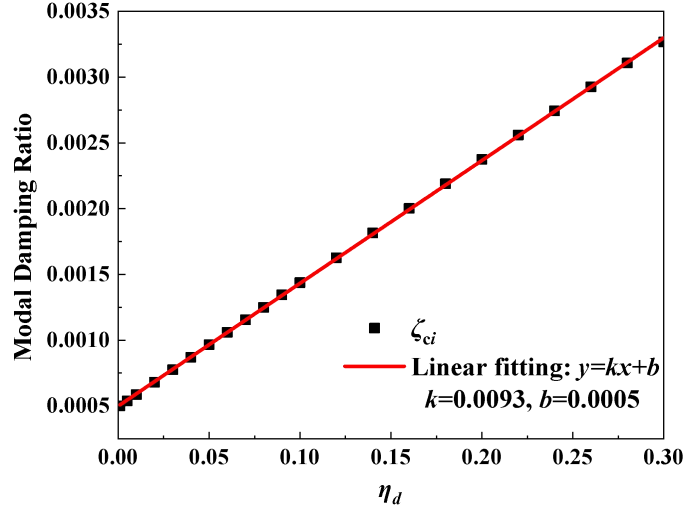
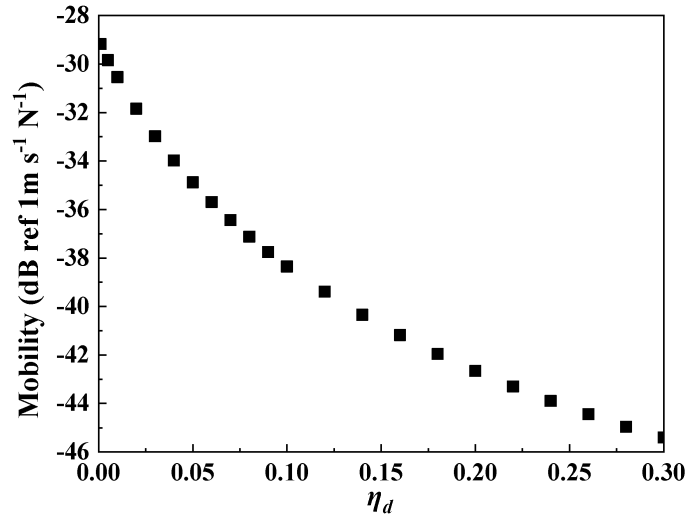


Fig.14. The relationship between the material loss factor of the coating layers and the modal damping of the ABH-DVA with the mode of R1C0 and R1C1



(a) Modal damping ratio of the primary structure with different  $\eta_d$



(b) Driving point mobility of the primary structure with different  $\eta_d$

Fig.15. Modal damping ratio and driving point mobility of the primary structure with different  $\eta_d$  at modal frequency of 640.1 Hz

#### 4. Experimental validation

Experiments were performed to validate the numerically predicted vibration suppression performance of the proposed 2D ABH-DVA. An aluminum ABH-DVA of the same size as the one used in the simulation was manufactured by computer numerical control (CNC) milling. A ring of butyl rubber damping layer with an outer diameter of 122 mm was pasted on the surface of the ABH-DVA. Three different damping layouts of the ABH-DVA were realized using different widths of the damping layer, namely 5 mm, 8 mm and 30 mm respectively, instead of using

different damping material. The primary structure is an aluminum plate of the same size as that used in the simulation. Free boundary condition was realized by suspending the plate using two elastic strings attached to a rigid frame. The ABH-DVA was installed on the primary plate via a standard 5 mm screw. The experimental setup is shown in Fig.16. An electromagnetic shaker (B&K 4809), driven by a power amplifier (B&K 2718), was used to generate a periodic chirp force from 10 Hz to 3000 Hz to excite the plate at (100, 50) mm. The response measurement was performed using a Polytec™ Laser Scanning Vibrometer (PSV 500) device.

The driving point mobility of the plate without and with ABH-DVA was measured up to 3000 Hz and the results are shown in Fig. 17. The upper limit frequency was set to 3000 Hz due to excitation and measurement limitations. It can be seen from Fig. 17(a), where the damping layer with the same width (30 mm) as that in simulations is pasted, that the deployment of the ABH-DVA indeed causes a vibration reduction in all resonant peaks in the measured frequency range. This validates the effectiveness of the 2D ABH-DVA in the vibration suppression of a 2D primary structure.

Due to the relatively large amount of damping materials bonded on the 2D ABH-DVA, all the resonance peaks have been effectively reduced so that the two control mechanisms are difficult to distinguish from the shape of peaks. In order to further verify the two control mechanisms of the 2D ABH-DVA, two cases with narrower damping strips were measured and shown in Fig. 17(b). More specifically, the dynamic interaction effect is observed at the resonance modes of the plate at 273.4 Hz, 592.2 Hz, 1314.1 Hz, 1759.4 Hz and 1965.6 Hz, and damping enhancement is observed in basically all other resonance mode, as shown in Fig. 17(b).

Results generally agree although rigorous comparison is difficult to achieve because of the uncertainties in the estimation of some physical parameters such as the frequency-dependent loss factors of the damping material to which dynamic interaction effect is very sensitive. Slight difference in resonance frequencies in the plate and ABH-DVA can also cause significant difference in the frequency response of the combined structure. In order to further investigate the cause that leads to the

observed differences, the mode shapes of the 2D ABH-DVA around these frequencies were measured and shown in Fig. 18. It follows that the actual ABH-DVA is not strictly axisymmetric due to the machining imperfection in the ABH-DVA on one hand, and the installation shaft connecting the primary structure with the add-on structure is not completely in the center of the ABH-DVA on the other hand. As a result, the mode shapes of the ABH-DVA are not as ideal as the simulation results. The real operational mode shapes observed experimentally are the result of regrouping the ideal modes caused by machining imperfection. For example, both modes at 212.5 Hz and 582.8 Hz are the combination of the modes R1C1 and R1C0, with the former more like the shape of R1C1 and the later more like the shape of R1C0. Obviously, the modes at 212.5 Hz and 582.8 Hz are coupled with the plate and induce the dynamic interaction effect at 273.4 Hz and 592.2 Hz. The reason for the dynamic interaction effect in the modes above 1000 Hz is believed to be the same. Despite of the imperfection, the vibration suppression performance predicted by numerical simulations, as well as the predicted coupling phenomena are both confirmed. Meanwhile, results also allude to the possibility of making use of the imperfection to deliberately destroy the axisymmetric property of the ABH-DVA in order to further improve the performance of the device. This should be explored in our future work.

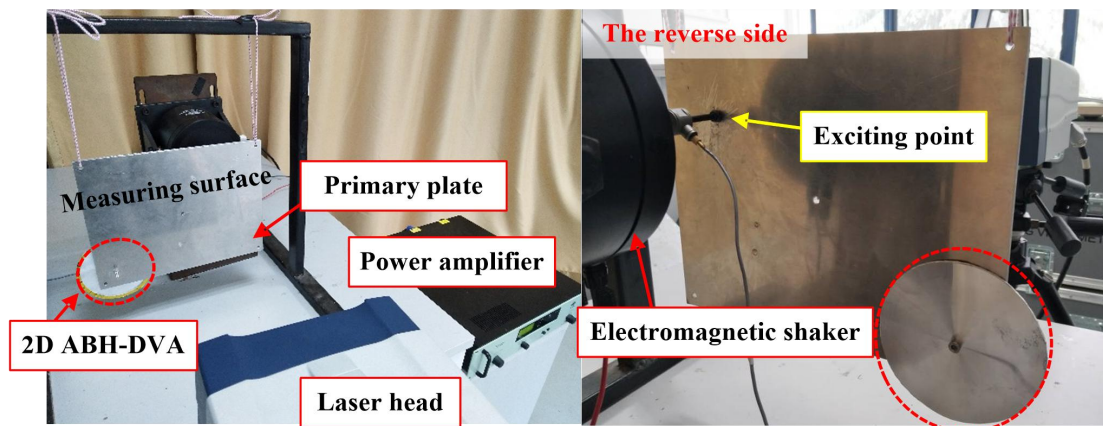
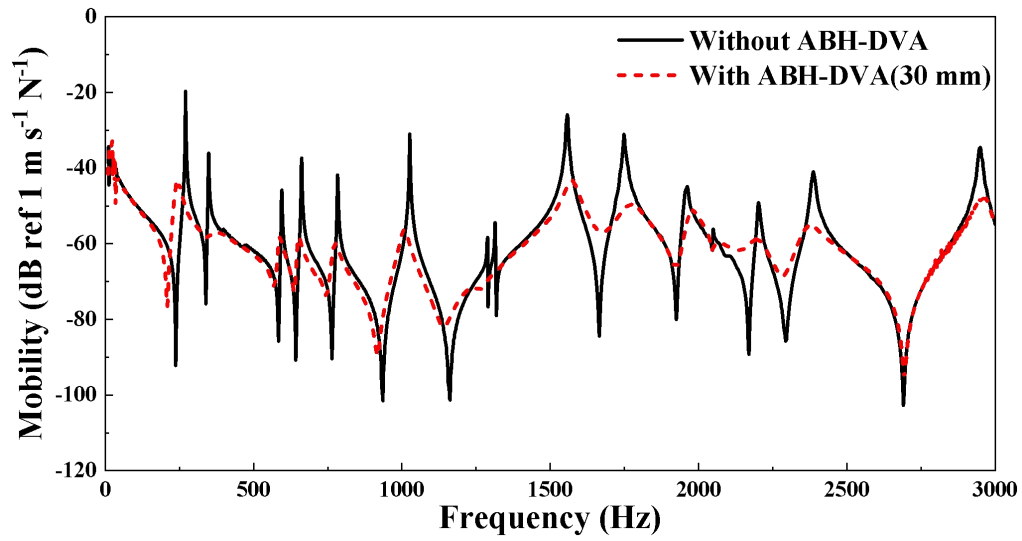
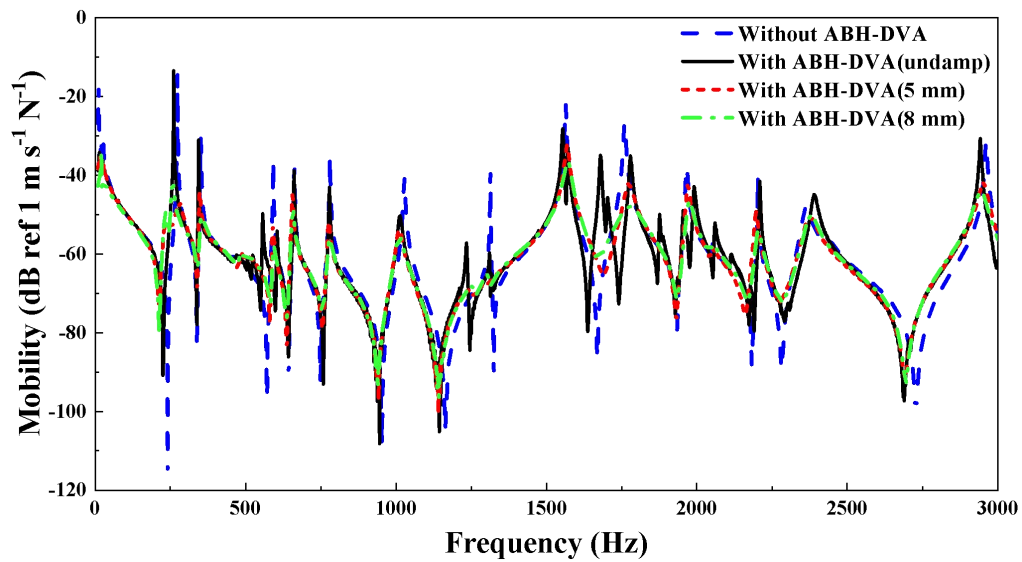


Fig.16. Experimental test set-up



(a)



(b)

Fig.17. Experimental results of driving point mobility of the plate without and with different ABH-DVAs: (a) with a wider damping layer; (b) with two narrower damping layers

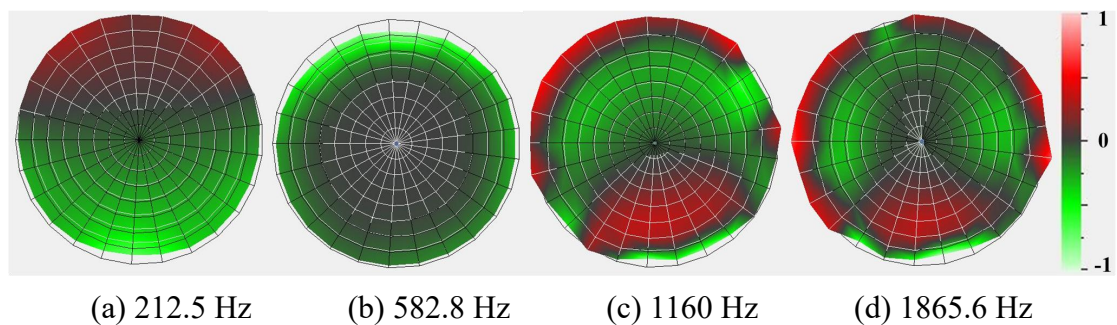


Fig.18. Experimentally measured mode shapes of the ABH-DVA

## 5. Conclusions

To tackle the inherent limitations of embedding ABH features into structures, this paper proposes a new type of 2D circular ABH-DVA as an auxiliary add-on device for the vibration suppression in a two-dimensional structure. Its design, dynamics and performance differ from the existing ones reported in the literature. Using a plate as benchmark structure, FE simulation results show a systematic reduction of the resonant peaks of the primary structure over a broad frequency range upon the deployment of the ABH-DVA.

Analyses based on a simplified, yet fully coupled model, explain the observed phenomena within specific frequency ranges and allow drawing design guidelines. In particular, a modal coupling coefficient is defined to evaluate the strength of the modal coupling, which is shown to play a vital role in system performance analysis. Analyses uncover two major vibration suppression mechanisms: dynamic interaction between the host structure and the ABH-DVA, and damping enhancement as a result of ABH-specific energy trapping of the latter, for different resonance modes of the primary structure. The occurrence of both physical mechanisms can be materialized provided that the strong coupling conditions are met, as quantified by the defined coupling coefficient. In this regard, the proposed 2D circular ABH-DVA features selective coupling pattern with the primary plate. Despite the abundant modes and the rich dynamic of the ABH-DVA, only a few of them (which feature  $n=0$  and 1 in the circumferential directions of the disk) are strongly coupled with the primary structure to trigger the two aforementioned mechanisms. The coupling coefficient between a mode of the primary structure and that of the ABH-DVA depends not only on the mode shape of the latter, but also its installation position.

Meanwhile, upon a proper coupling, the low-frequency modes of the ABH-DVA that strongly couple with the primary structure contribute to a damping increase of the primary structure with higher resonance frequencies due to the ABH effect. The aggregated damping enhancement on most of structural modes, alongside the effective dynamic interaction on particular modes, collectively contribute to a broadband overall reduction of the system resonances, as confirmed both numerically

and experimentally in this paper.

As a future work, the vibration suppression performance of the proposed device can be further improved by optimizing its geometry parameters and the profile.

## Acknowledgements

This research was supported by the National Natural Science Foundation of China (No. 52022039 & 51775267 & 11532006), the Research Grants Council of Hong Kong Special Administrative Region, China (PolyU 152017/17E), and A Project Funded by the Priority Academic Program Development of Jiangsu Higher Education Institutions.

## Reference

- [1] V. V. Krylov, F.J.B.S. Tilman, Acoustic “black holes” for flexural waves as effective vibration dampers, *J. Sound Vib.* 274 (2004) 605–619. <https://doi.org/10.1016/j.jsv.2003.05.010>.
- [2] V. V. Krylov, New type of vibration dampers utilising the effect of acoustic “black holes,” *Acta Acust. United with Acust.* 90 (2004) 830–837. <https://www.researchgate.net/publication/233521336>.
- [3] W. Huang, H. Ji, J. Qiu, L. Cheng, Wave Energy Focalization in a Plate With Imperfect Two-Dimensional Acoustic Black Hole Indentation, *J. Vib. Acoust. Trans. ASME.* 138 (2016) 1–12. <https://doi.org/10.1115/1.4034080>.
- [4] V. V. Krylov, R.E.T.B. Winward, Experimental investigation of the acoustic black hole effect for flexural waves in tapered plates, *J. Sound Vib.* 300 (2007) 43–49. <https://doi.org/10.1016/j.jsv.2006.07.035>.
- [5] V. Kralovic, V. V. Krylov, Damping of flexural vibrations in tapered rods of power-law profile: Experimental studies, *Proc. Inst. Acoust.* 29 (2007) 66–73. <https://www.researchgate.net/publication/281976853>.
- [6] L. Tang, L. Cheng, H. Ji, J. Qiu, Characterization of acoustic black hole effect using a one-dimensional fully-coupled and wavelet-decomposed semi-analytical model, *J. Sound Vib.* 374 (2016) 172–184. <https://doi.org/10.1016/j.jsv.2016.03.031>.
- [7] J.J. Bayod, Experimental study of vibration damping in a modified elastic wedge of power-law profile, *J. Vib. Acoust. Trans. ASME.* 133 (2011) 1–7. <https://doi.org/10.1115/1.4003591>.
- [8] M. Shepherd, C. McCormick, S. Conlon, P. Feurtado, Modeling and optimization of acoustic black hole vibration absorbers, *J. Acoust. Soc. Am.* 141 (2017) 4034. <https://doi.org/10.1121/1.4989305>.
- [9] C. McCormick, M. Shepherd, Design optimization and performance comparison of three styles of one-dimensional acoustic black hole vibration absorbers, *J. Sound*

- Vib. 470 (2019) 115164. <https://doi.org/10.1016/j.jsv.2019.115164>.
- [10] L. Ma, H.-W. Dong, L. Cheng, An Alternative and Optimized Thickness Profile of an Acoustic Black Hole Plate, *J. Sound Vib.* 486 (2020) 115619. <https://doi.org/10.1016/j.jsv.2020.115619>.
- [11] J.J. Bayod, Application of elastic wedge for vibration damping of turbine blade, *MOVIC 2010 - 10th Int. Conf. Motion Vib. Control. Proc.* 5 (2010) 1167–1175. <https://doi.org/10.1299/jsdd.5.1167>.
- [12] E.P. Bowyer, V. V. Krylov, Experimental investigation of damping flexural vibrations in glass fibre composite plates containing one- and two-dimensional acoustic black holes, *Compos. Struct.* 107 (2014) 406–415. <https://doi.org/10.1016/j.compstruct.2013.08.011>.
- [13] E.P. Bowyer, V. V. Krylov, Experimental study of sound radiation by plates containing circular indentations of power-law profile, *Appl. Acoust.* 88 (2015) 30–37. <https://doi.org/10.1016/j.apacoust.2014.07.014>.
- [14] E.P. Bowyer, V. V. Krylov, A review of experimental investigations into the acoustic black hole effect and its applications for reduction of flexural vibrations and structure-borne sound, *INTER-NOISE 2015 - 44th Int. Congr. Expo. Noise Control Eng.* (2015). <https://www.researchgate.net/publication/282186765>.
- [15] L. Zhao, S.C. Conlon, F. Semperlotti, Broadband energy harvesting using acoustic black hole structural tailoring, *Smart Mater. Struct.* 23 (2014). <https://doi.org/10.1088/0964-1726/23/6/065021>.
- [16] L. Zhao, S.C. Conlon, F. Semperlotti, An experimental study of vibration based energy harvesting in dynamically tailored structures with embedded acoustic black holes, *Smart Mater. Struct.* 24 (2015). <https://doi.org/10.1088/0964-1726/24/6/065039>.
- [17] L. Tang, L. Cheng, Ultrawide band gaps in beams with double-leaf acoustic black hole indentations, *J. Acoust. Soc. Am.* 142 (2017) 2802–2807. <https://doi.org/10.1121/1.5009582>.
- [18] T. Zhou, L. Tang, H. Ji, J. Qiu, L. Cheng, Dynamic and Static Properties of Double-Layered Compound Acoustic Black Hole Structures, *Int. J. Appl. Mech.* 9 (2017) 1–18. <https://doi.org/10.1142/S1758825117500740>.
- [19] V.B. Georgiev, J. Cuenca, F. Gautier, L. Simon, V. V. Krylov, Damping of structural vibrations in beams and elliptical plates using the acoustic black hole effect, *J. Sound Vib.* 330 (2011) 2497–2508. <https://doi.org/10.1016/j.jsv.2010.12.001>.
- [20] E.P. Bowyer, D.J. O’Boy, V. V. Krylov, F. Gautier, Experimental investigation of damping flexural vibrations in plates containing tapered indentations of power-law profile, *Appl. Acoust.* 74 (2013) 553–560. <https://doi.org/10.1016/j.apacoust.2012.10.004>.
- [21] E.P. Bowyer, P. Nash, V. V. Krylov, Damping of flexural vibrations in glass fibre composite plates and honeycomb sandwich panels containing indentations of power-law profile, *Proc. Meet. Acoust.* 18 (2012). <https://doi.org/10.1121/1.4776154>.
- [22] T. Zhou, L. Cheng, A resonant beam damper tailored with Acoustic Black Hole features for broadband vibration reduction, *J. Sound Vib.* 430 (2018) 174–184. <https://doi.org/10.1016/j.jsv.2018.05.047>.

[23] V. Denis, A. Pelat, F. Gautier, B. Elie, Modal Overlap Factor of a beam with an acoustic black hole termination, *J. Sound Vib.* 333 (2014) 2475–2488.

<https://doi.org/10.1016/j.jsv.2014.02.005>.

[24] P. He, X. Wang, H. Ji, J. Qiu, L. Cheng, Full-band vibration control of box-type structure with acoustic black hole, *Acta Aeronautica et Astronautica Sinica*. 41 (2020) 223350. <https://doi.org/10.7527/S1000-6893.2019.23350>. (in Chinese)